



ELSEVIER

Ultramicroscopy 59 (1995) 195–213

---

---

**ultramicroscopy**

---

---

## Delocalization in inelastic scattering

D.A. Muller <sup>a</sup>, J. Silcox <sup>b</sup><sup>a</sup> *Physics Department, Cornell University, Ithaca, NY 14853, USA*<sup>b</sup> *School of Applied and Engineering Physics, Cornell University, Ithaca, NY 14853, USA*

Received 27 September 1994; in final form 26 January 1995

---

### Abstract

How delocalized is an EELS signal? For instance, how far from a silicon atom must the electron probe be before a Si edge can be detected? A crude estimate of a localization length ( $\lambda/\theta_E$ ) suggests a maximum impact parameter of 50 Å for a typical plasmon loss. Yet with care, subnanometer resolution plasmon maps can be achieved. The improved resolution cannot be accounted for by dielectric screening as the dielectric screening length diverges for energy losses at and above the plasmon frequency. Niels Bohr [1] offered a classical explanation in 1913 leading to his adiabatic criterion for a cutoff impact parameter  $b_{\max} = v/\omega$ , for a fast electron, velocity  $v$ , and an energy loss of frequency  $\omega$ . By starting with a quantum mechanical expression for the energy loss, both the semiclassical limit and surprisingly Bohr's criterion can be recovered and are found to be in excellent quantitative agreement with experiment. We show  $b_{\max}$  can be thought of as a “dynamic” screening length and plays the same role as the screening length does in the elastic scattering from a Thomas–Fermi atom. In fact the parallel component of the inelastic scattering has the same form as elastic scattering from a Thomas–Fermi atom and much of our understanding of the role of the detector in annular dark-field imaging can be applied here. However, in inelastic scattering a dramatic improvement in resolution can be obtained with an off-axis detector as suggested by Ritchie and Howie [2]. Here we present experimental evidence of such an effect.

---

### 1. Introduction

Inelastic electron scattering is often viewed as a delocalized process, especially for small energy losses. Bohr's adiabatic criterion [1] suggests a maximum impact parameter of 50 Å for a typical plasmon loss yet Fig. 1 shows 8 Å resolution can be achieved. Earlier work by Scheinfein and Isaacson [3] and Colliex et al. [4] have reported similar results. Kohl and rose [5] have used the first Born approximation to calculate the intensity distribution expected for plasmon images in a conventional transmission electron microscope (CTEM) and a scanning transmission electron

microscope (STEM). They also find the scattering to be more localized than the rule-of-thumb argument might suggest. Ritchie and Howie [2] have shown that the first Born approximation reduces to a semiclassical description of inelastic electron scattering in a STEM with a very large detector. In this case they find an incoherent imaging results where the incident probe intensity is convolved with the inelastic response from a classical electron to form the final image. Although in experiments the collector is often the same size as the objective aperture, the semiclassical description seems to show the same trends as seen experimentally [6–8] at least at greater than a

nanometer length scale. Kohl and Rose [5] find that the intensity distribution for a small collector or for a CTEM is dramatically different from the semiclassical limit, especially for length scales smaller than 1 nm. This is of some concern as it is becoming more common to perform EELS (electron energy loss spectroscopy) using atomic-sized probes with STEMs [9–11] and similar conditions may yet be reached in the new generation of CTEMs equipped with field emission guns.

The earliest semiclassical calculation (a classical electron exciting a quantum system) is due to Fermi in 1924 [12]. Mott [13] and Frame [14] showed that the impact parameter integration of Gaunt [15] is equivalent to Bethe's results using plane waves [16]. This derivation for scattering from a single dipole is reviewed in Bolton and Brown [17] as are some more complicated geometries. Calculations have also been made for other specimen shapes such as spheres, semi-infinite planes, and planar interfaces [18,19,2].

The main difficulties in making quantitative comparisons with theory have been the very weak signals involved, uncertainties in the shape of the specimen and position of the probe. By using single electron pulse counting and simultaneously recording the annular dark-field (ADF) signal with the energy loss spectrum we are able to make quantitative comparisons of theory with experiments performed using a STEM. In partic-

ular we find that a novel off-axis collector scheme suggested by Ritchie and Howie [2] does lead to an improved spatial resolution in energy loss imaging. The improvement is dramatic, allowing the plasmon image to have the same resolution as the ADF image recorded simultaneously. After reviewing the classical, and quantum theories of delocalization in inelastic scattering, we calculate the expected off-axis collector resolution and find it to be in good agreement with the unexpected experimental results. A very simple explanation can be found within the quantum treatment and is best understood as an inelastic "weak beam" imaging. Some more typical instrument geometries are also considered such as a STEM with a very large or very small detector. The large collector limit leads to incoherent imaging from which the semiclassical limit can be recovered were the probe is treated classically. For the small collector limit (which is similar to conditions in a CTEM) wave-like properties of the probe become important. The difference in measured signals is essentially an illustration of the wave-particle duality of the electron wavepacket.

## 2. Classical theory

Classically the energy loss of a swift electron, velocity  $v$ , passing a bound electron at impact

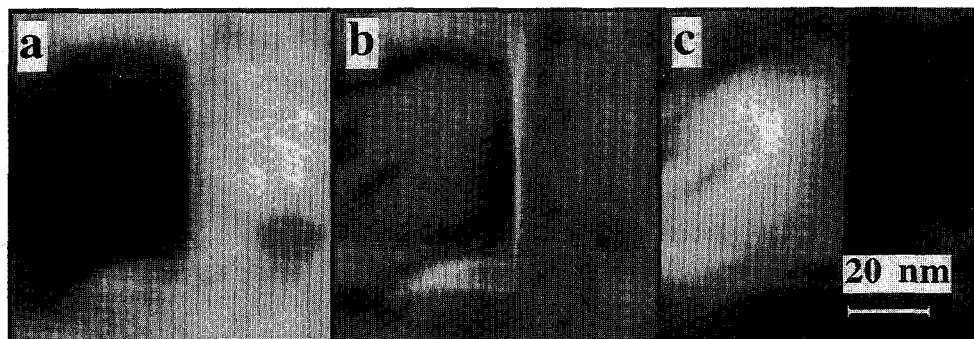


Fig. 1. Plasmon loss maps of a diamond grain (left of each image) embedded in a ZnS matrix. Images recorded on a VG STEM with a 100 kV beam,  $C_s = 3.3$  mm, 10 mrad objective and collector apertures and a 5 ms dwell time per pixel. (a) ZnS bulk plasmon loss at 18 eV, (b) a-C or diamond surface plasmon at 25 eV and (c) diamond bulk plasmon at 34 eV. Specimen supplied by Yujiun Tzou.

parameter  $b$  is given in the impulse approximation as [1,20]

$$\Delta E(b) = \frac{2e^4}{mv^2} \left( \frac{1}{b^2} \right). \quad (1)$$

This expression is valid provided the collision time  $b/v$  is short compared to the restoring period of the bound electron  $1/\omega$  (i.e. the electric field generated by the swift electron is above the resonance frequency of the bound electron). When the collision time is longer, the bound electron can follow the time varying field and remains bound so the interaction is adiabatic. The crossover at  $b_{\max} = v/\omega$  is Bohr's cutoff beyond which the target is "dynamically screened". The dynamical screening arises from the more slowly varying electric field seen at large distances, rather than any property of the intervening medium and so will be expected in free space as well.

The classical result for  $\Delta E(b)$  is not correct quantum mechanically since not every collision at  $b$  loses an energy  $\Delta E(b)$ , but rather has a different probability  $P(b, E)$  of losing a discrete amount of energy  $E$  at different  $b$ . For a large number of collisions, the average energy loss at  $b$  will be  $P(b, E) \cdot E$  quantum mechanically and  $\Delta E(b)$  classically. In the limit where the incident electron can be treated as a classical particle, the correspondence principle requires  $P(b, E_i) = \Delta E(b)/E_i$  so  $P(b, E) \propto 1/b^2$  for  $b < b_{\max}$  and is rapidly damped for  $b > b_{\max}$ . Since the  $1/b^2$  dependence came from considering only the dipole contribution of the time-varying electric field and Bohr's argument must hold for any multipole field,  $P(b, E)$  at large  $b$  must decay faster than any power law. So we might in fact expect this dynamic screening will lead to an exponential decay at large distances.

Some hint of this can be seen in the classical expression for energy transfer from a fast electron to a harmonically bound charge with resonant frequency  $\omega$ . The spatial dependence of the energy transfer can be found by Fourier-analyzing the time-varying dipole field of the fast electron to give (see Chapter 13.2 of Jackson [20] –

we give the non-relativistic expression here although relativistic corrections are important; their main effects are changing  $b_{\max}$  to  $b_{\max} = \gamma v/\omega$  and reducing the parallel to perpendicular components by  $1/\gamma^2$ )

$$\Delta E(b) = \frac{2e^4}{mv^2} \left( \frac{1}{b_{\max}} \right)^2 \times [K_0^2(b/b_{\max}) + K_1^2(b/b_{\max})]. \quad (2)$$

$K_0$  and  $K_1$  are modified Bessel functions which decay asymptotically as  $K_n(x) \propto e^{-x}/\sqrt{x}$  for large  $x$ . So when  $b \gg b_{\max}$ , the classical energy loss and the corresponding quantum mechanical signal  $P(b, E)$  should decay exponentially with a screening length  $b_{\max}/2$ . The impulse approximation is recovered for small distances as then  $K_1(x) \propto 1/x$  so  $\Delta E(b) \propto 1/b^2$ . This diverges at the origin classically as the electron is treated as a point charge. Quantum mechanically we would expect  $P(b, E) \propto 1/b^2$  so long as  $b$  is larger than the shortest wavelengths in the electron wave packet.

### 3. Quantum theory

The semiclassical models where the incident electron is treated as a classical point charge while the interactions with the target are treated quantum mechanically should be an adequate description of the delocalization provided the probe width is much smaller than the impact parameter and all the scattered electrons are collected. Again when the probe is much larger than the target then using a single plane wave in first Born approximation is sufficient to calculate the quantum mechanical cross section.

If the probe is of the same dimensions as the target then the probe wave function  $a(\mathbf{r} - \mathbf{b})$  cannot be treated as a single plane wave and must be Fourier-analyzed in its components  $A(k)$ . Such a calculation is given in Appendix A where the scattering is treated within the first Born approximation and the momentum transfer is assumed to be small. As this is a first-order perturbation theory, the probe and the target interact linearly

so  $P(b, E)$  can be expressed as a convolution of real spaces variables (Eq. (A.22)):

$$P(b, E) = \frac{4R_y}{E_0} \int a(\boldsymbol{\rho} - \mathbf{b}) a^*(\boldsymbol{\rho}' - \mathbf{b}) \times w(\boldsymbol{\rho}, \boldsymbol{\rho}', E) D(\boldsymbol{\rho} - \boldsymbol{\rho}') d^2\rho d^2\rho'. \quad (3)$$

$w(\boldsymbol{\rho}, \boldsymbol{\rho}', E)$  is a transmission function of sorts called the “cross spectral object transparency” by Rose [21] (specific forms of  $w(\boldsymbol{\rho}, \boldsymbol{\rho}', E)$  are discussed in Appendix B).  $P(b, E)$  depends on the probe wave functions, rather than their amplitudes so coherence effects might be expected. The detector function  $D(\boldsymbol{\rho} - \boldsymbol{\rho}')$  can mix signals from different  $\boldsymbol{\rho}, \boldsymbol{\rho}'$  so it affects the size of the coherence volume. This is best illustrated by considering the (not so) special case of a circular collector centered on the optic axis so

$$D(\boldsymbol{\rho} - \boldsymbol{\rho}') = \frac{2\pi\beta_0^2 J_1(k_0\beta_0|\boldsymbol{\rho} - \boldsymbol{\rho}'|)}{k_0\beta_0|\boldsymbol{\rho} - \boldsymbol{\rho}'|}. \quad (4)$$

This can be simplified further for the two limiting cases  $k_0\beta_0|\boldsymbol{\rho} - \boldsymbol{\rho}'| \gg 1$  and  $k_0\beta_0|\boldsymbol{\rho} - \boldsymbol{\rho}'| \ll 1$ . Since the spatial extent of  $|\boldsymbol{\rho} - \boldsymbol{\rho}'| \approx 1/\theta_0$  (from the overlap of the probe wave functions), the first case becomes  $\beta_0 \gg \theta_0$  and the second  $\beta_0 \ll \theta_0$  i.e. *the limits are for a STEM with large and small collector apertures, respectively*. The large collector limit leads to incoherent imaging and can be reduced to the semiclassical limit where the probe can be treated classically while wave-like properties of the probe become important for the small collector limit (which is similar to conditions in a CTEM).

### 3.1. Incoherent imaging with a large detector

For large  $k_0\beta_0$  Eq. (4) becomes

$$D(\boldsymbol{\rho} - \boldsymbol{\rho}') \Rightarrow 2\pi\beta_0^2 \delta(|\boldsymbol{\rho} - \boldsymbol{\rho}'|), \quad (5)$$

which allows Eq. (3) to be rewritten as a convolution of the probe intensity with the cross spectral transparency function:

$$P(b, E) = \frac{4R_y}{E_0} |a(\mathbf{b})|^2 \otimes w(\boldsymbol{\rho}, \boldsymbol{\rho}, E). \quad (6)$$

For a classical electron  $|a(\mathbf{b})|^2 = \delta(\mathbf{b})$  so  $P(b, E) \propto w(b, b, E)$ . The diagonal terms of the cross spectral object transparency can then be identified with the probability for an energy loss  $E$  of a classical electron at  $b$  from a quantum excitation of the specimen. To compare Eq. (6) with the classical discussion it is useful to have an explicit form for  $w(\boldsymbol{\rho}, \boldsymbol{\rho}', E)$  and the simplest case is that for a dipole transition (see Appendix B). Throughout the theory section of this paper we will consider only the response from a single dipole for illustrative purposes. The appropriate quantum mechanical form for an assembly of independent scatterers can be found in Ref. [5] and a simple model of a surface plasmon is given in Ref. [2].

Writing  $z_{\text{fi}}$  and  $x_{\text{fi}}$  as the parallel and perpendicular components of the dipole matrix elements  $\mathbf{r}_{\text{if}} = \langle \varphi_f | \mathbf{r} | \varphi_i \rangle$  then substituting  $w(\boldsymbol{\rho}, \boldsymbol{\rho}, E)$  from Eq. (B.10) into (6) and noting that  $k_0\theta_E = 1/b_{\text{max}}$  we get

$$P_D(b, E) = \left( \frac{R_y}{E_0} \right)^2 \left( \frac{1}{b_{\text{max}}} \right)^2 \left[ |K_0(b/b_{\text{max}})z_{\text{fi}}|^2 + |K_1(b/b_{\text{max}})x_{\text{fi}} \cos \gamma|^2 \right]. \quad (7)$$

This is proportional to  $\Delta E(b)$ , the classical energy loss from a dipole, discussed in Section 2 which must be expected from the correspondence principle. The result is not classical. Although we know where the electron scattered (it was at impact parameter  $b$ ), we do not know the scattering angle (i.e. the momentum transfer). This is because the correspondence with the classical swift particle could only be made when the detector was chosen to accept electrons scattered to all angles ( $\beta_0 \rightarrow \pi$  in Eq. (5)). If a small collector is used, then wave-like (interference) effects can be observed.

A semiclassical result similar to Eq. (7) was first deduced by Fermi [12] by Fourier-decomposing the electric field of the swift electron as was done for the classical argument leading to Eq. (2). However, he realized that the coupling of each component of the time-varying electric field to the target was the same as that for X-rays of

equivalent frequency. For an isotropic material with X-ray absorption coefficient  $\alpha(\omega)$  he found  $P_D(b, E)$

$$\propto \left( \frac{1}{b_{\max}} \right)^2 [K_0^2(b/b_{\max}) + K_1^2(b/b_{\max})] \alpha(\omega). \quad (8)$$

The spatial dependence of a given energy loss is then independent of the details of the absorption coefficient and depends only on the frequency. (This holds exactly at and above the plasmon frequency since plasmons cannot screen themselves.) Fermi's argument led to the method of "effective photons" pioneered by Weizsäcker and Williams [20,22] where the energy loss of charged particles is analyzed in terms of the equivalent photon field from that moving charge. This is often exploited in nuclear physics [23] to generate very high energy intense bursts of effective photons by scattering highly charged particles at small impact parameters.

The equivalent photon field turns out to be short-ranged and for a very simple reason. The fast electrons in the incident probe are assumed to be travelling in a straight line and an electric charge travelling along a straight line at a constant velocity  $v$  is strictly forbidden from radiating. Instead the time-varying electric field generated by the probe,  $E(\omega, b)$  must be short-ranged and evanescent (see Jackson's Eq. (13,29–30) [20]). The decay length of the evanescent field at frequency  $\omega$  for an electron with velocity  $v$  can also be deduced on dimensional grounds to be  $b_{\max} = v/\omega$  since the only relevant physical parameters are  $v$  and  $\omega$ . This is not surprisingly the same as the  $b_{\max}$  obtained from Bohr's adiabatic argument. In fact the modified Bessel functions  $K_0$  and  $K_1$  in Eqs. (8) or (9) result from having effectively calculated the components of the dipole field  $E_D(\omega, b)$  parallel and perpendicular to the probe. (For instance the electric field perpendicular to a swift electron travelling in a straight line is

$$E_{\perp}(\omega, b) = e/bv\sqrt{2/\pi} [(b/b_{\max})K_1(b/b_{\max})] \\ \propto e^{-b/b_{\max}}$$

[20]. As a reality check  $b_{\max}(=v/\omega) \rightarrow \infty$  as  $\omega \rightarrow 0$  so the static field  $E_{\perp}(0, b) \propto 1/b$  which is long-ranged as expected.)

The implications of the dimensional argument are twofold. Firstly, *the inelastic interaction of the swift electron with the specimen is inherently short-ranged*. Secondly, the behaviour of the scattering at large distances is dominated by the kinematics of the scattering (through  $b_{\max}$  and hence the energy loss) rather than any special property of the specimen.

Returning to Eq. (6), we now see it has the same functional form as that found by Ritchie and Howie [2] where the incident probe intensity is convolved with the inelastic response from a classical electron to form the final image. Substituting (B.10) into (6) we find for scattering from a dipole:

$$P_D(b, E) = \frac{\beta_0^2 R_y}{\pi^2 E_0} |a(\mathbf{b})|^2 \\ \otimes \left( \frac{1}{b_{\max}} \right)^2 \left[ |K_0(b/b_{\max})z_{\text{fi}}|^2 \right. \\ \left. + |K_1(b/b_{\max})x_{\text{fi}} \cdot \cos \gamma|^2 \right]. \quad (9)$$

The first term,  $K_0^2(b/b_{\max})$ , arises from excitations parallel to the swift electron's trajectory while the second term contains contributions from perpendicular excitations (i.e. transverse fields). The classical discussion of Eq. (1) which deduced the two limits of  $K_1^2(b/b_{\max})$  considered only excitations perpendicular to the swift electron. At small distances the perpendicular excitations dominate and  $P(b, E) \propto 1/b^2$  while at large distances the parallel and perpendicular components are comparable and both decay similarly so  $P(b, E) \propto \exp(-2b/b_{\max})$ . The crossover occurs at Bohr's adiabatic limit  $b_{\max}$ . Notice that for any multipole approximation the spatial dependence is determined only by the energy loss (through  $b_{\max}$ ) and not by the matrix elements  $z_{\text{if}}^n = \langle \varphi_f | z^n | \varphi_i \rangle$ . Once a multipole approximation has been made, the matrix elements determine only the overall intensity and it is the multipole electric field that decides the spatial dependence as would be expected from correspondence with the

classical argument. The exponential decay at large distances is more general than the multipole approximation as it relies only on the effective photon field being evanescent.

### 3.2. Coherent imaging with a small detector on axis

For a small collector aperture, Eq. (4) becomes

$$D(\boldsymbol{\rho} - \boldsymbol{\rho}') = \frac{2\pi\beta_0^2 J_1(k\beta_0 |\boldsymbol{\rho} - \boldsymbol{\rho}'|)}{k\beta_0 |\boldsymbol{\rho} - \boldsymbol{\rho}'|} \rightarrow \pi\beta_0^2, \quad (10)$$

which allows an unrestricted integral over  $\boldsymbol{\rho}$  and  $\boldsymbol{\rho}'$  so the coherence volume is effectively the entire specimen. Using Eq. (B.9) for  $w(\boldsymbol{\rho}, \boldsymbol{\rho}', E)$  and Eq. (10) for  $D(\boldsymbol{\rho} - \boldsymbol{\rho}')$  Eq. (3) to be rewritten as

$$P_D(b, E) = \frac{\beta_0^2}{2\pi^2} \frac{R_y}{E_0} \left( \frac{1}{b_{\max}} \right)^2 |a(\mathbf{b}) \otimes [K_0(k_0\rho\theta_E)z_{\text{fi}} + iK_1(k_0\rho\theta_E)x_{\text{fi}} \cos \gamma]|^2 \quad (11)$$

provided  $k_0\rho \gg 1$ . The resultant image is coherent as the probe wave function, rather than the probe intensity, has been convolved with the transmission function and contrast reversals are possible for defocused probes or when additional elastic scattering is considered. The scattering probabilities calculated throughout this paper consider the inelastic scattering only and ignore the possibility of plural scattering. However, as the elastic scattering cross section is larger than the inelastic one, it cannot be ignored. If we consider only a single inelastic scattering event, then the incident unscattered beam can be filtered out and no phase contrast image can be formed. When even single elastic scattering is allowed, then interference between the elastically + inelastically scattered beam and the inelastic only beam will give rise to a phase contrast image. The contrast of the elastic image will be preserved in the inelastic image, provided the inelastic scattering angle is small enough that it can still be thought of as the analog of the unscattered beam for elastic scattering [24].

### 3.3. Limits of the semiclassical approximation

The semiclassical forms given above must fail at small distances as the scattering probability does not become infinite. (Classically we know the energy loss of Eqs. (1) or (2) cannot exceed that of the incident electron and a number of approximations we have made no longer apply.) The dipole approximation (or any multipole expansion) assumes the probe electron is at an impact parameter much larger than the length of the dipole and this is usually taken as the cut off length to avoid the divergence in the resulting cross section [22]. The validity of the dipole approximation is discussed at the end of Appendix B. A more serious source of error, as will be seen when considering the small detector case, is that of treating the electron as a classical point charge. To recover the classical behavior in the present work we had to assume  $k_0\rho \gg 1$  in Eq. (B.7) and use the integral of Eq. (B.8) to obtain the modified Bessel function. Integrating  $x = k_0\rho\alpha$  to infinity can only be done for distances greater than the wavelengths contained in the electron wavepacket. At the origin, instead of a divergence we find

$$\lim_{\boldsymbol{\rho}, \boldsymbol{\rho}' \rightarrow 0} w(\boldsymbol{\rho}, \boldsymbol{\rho}', E) = \frac{(k_0\theta_E)^2}{2\pi} \log^2 \left[ 1 + \left( \frac{\alpha_0^2}{\theta_E^2} \right) \right] |z_{\text{fi}}|^2, \quad (12)$$

so the parallel component has tended to a constant value while the perpendicular contribution has vanished, even though for  $1/k_0 < b < b_{\max}$  it was the dominant component. This is essentially the origin of the donut-shaped response reported by Kohl and Rose [5] for the small collector case or CTEM (see also Fig. 2). To see why this donut shape does not also apply to the large collector it is useful to return to Eq. (A.17) and calculate the  $P(b, E)$  for an arbitrary detector geometry.

### 3.4. General detector geometries

At small distances the semiclassical approximation breaks down and we must return to the most general (but messiest) form of Eq. (A.17).

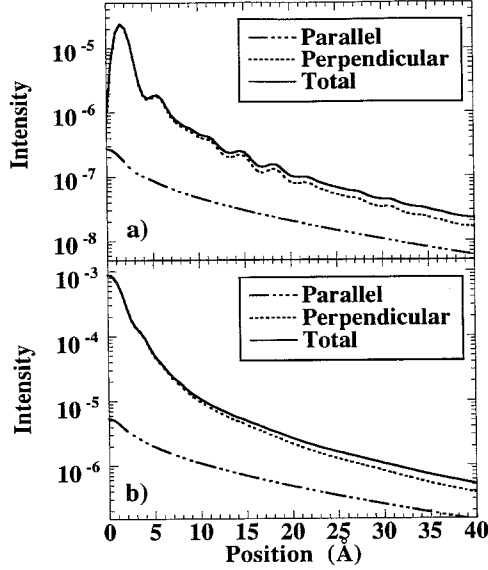


Fig. 2. Spatial distribution of the probability for a 25 eV energy loss by a 100 keV electron beam in a STEM with  $C_s = 1.3$  mm, 700 Å defocus and a 10 mrad objective aperture; (a) for a 1.6 mrad collector aperture and (b) for a 10 mrad collector aperture. The dotted line shows the component of  $P(b, E)$  perpendicular to the optic axis while the dot-dashed line shows the  $P(b, E)$  along the optic axis.  $b_{\max}$  is at 43 Å but the semiclassical approximation holds to within 5 Å of the dipole where the “donut” shape appears.

Keeping only the dipole component of  $\rho(\mathbf{K})_{i,f}$  then  $P(b, E)$  for an arbitrary detector geometry is:

$$P(b, E) = \frac{k_0^4 R_y}{4\pi^4 E_0} \int d^2\boldsymbol{\beta} D(\boldsymbol{\beta}) \left[ \theta_E^2 |A_{\parallel}(k_0 z_{\text{fi}})|^2 + \left\{ \begin{array}{l} \beta^2 |A_{\parallel}|^2 + |A_{\perp x}|^2 + |A_{\perp y}|^2 \\ -\beta_x (A_{\perp x} A_{\parallel}^* + A_{\perp x}^* A_{\parallel}) \\ -\beta_y (A_{\perp y} A_{\parallel}^* + A_{\perp y}^* A_{\parallel}) \end{array} \right\} \right] \times |(k_0 x_{\text{fi}})|^2, \quad (13)$$

where in the small-angle approximation  $\mathbf{K} = k_0[\theta_E \hat{z} + (\boldsymbol{\beta} - \boldsymbol{\theta})]$  so

$$A_{\perp x} = \int d^2\boldsymbol{\theta} A(\boldsymbol{\theta}) V(\mathbf{K}) \theta_x \exp(ik_0 \mathbf{b} \cdot \boldsymbol{\theta}) \quad (14)$$

and

$$A_{\parallel} = \int d^2\boldsymbol{\theta} A(\boldsymbol{\theta}) V(\mathbf{K}) \exp(ik_0 \mathbf{b} \cdot \boldsymbol{\theta}). \quad (15)$$

(Note that Eqs. (13–15) are non-relativistic. The main relativistic correction is the “pancaking” of the electric field so  $A_{\parallel}$  should be replaced by  $A_{\parallel}/\gamma$  throughout and  $k_0 \theta_E \rightarrow \gamma k_0 \theta_E$ . This can have a large effect on angle-resolved experiments.)

$4\pi e^2 V(\mathbf{K})$  is the Fourier transform of the Coulomb potential, i.e. the inelastic form factor:

$$4\pi e^2 V(\mathbf{K}) = \frac{4\pi e^2}{K^2} = \frac{4\pi e^2}{k_0^2 (\theta_E^2 + (\boldsymbol{\beta} - \boldsymbol{\theta})^2)}. \quad (16)$$

In general Eq. (13) must be integrated numerically, but for the limiting case of a very small detector on axis (i.e.  $\boldsymbol{\beta} \rightarrow 0$ )

$$P(b, E) = \frac{\beta_0^2 R_y}{\pi^2 E_0} \left[ \theta_E^2 |A_{\parallel 0}(k_0 z_{\text{fi}})|^2 + |A_{\perp 0}|^2 |k_0 x_{\text{fi}}|^2 \right], \quad (17)$$

where

$$A_{\perp 0} = \frac{1}{\theta_0} \int_0^{\theta_0} d\theta e^{ix(\theta)} \frac{\theta}{\theta_E^2 + \theta^2} J_1(ik_0 b\theta) \quad (18)$$

and

$$A_{\parallel 0} = \frac{1}{\theta_0} \int_0^{\theta_0} d\theta e^{ix(\theta)} \frac{1}{\theta_E^2 + \theta^2} J_0(ik_0 b\theta). \quad (19)$$

Unlike the semiclassical calculation for the small detector (Eq. (11)), Eqs. (17)–(19) will give the correct spatial dependence at small distances. Although derived for a STEM with a small collector, this is very similar to the CTEM result found in Kohl and Rose [5] (their Eq. (58)). As they discuss, the differences between the STEM and CTEM are the change in wavelength from  $k_0$  to  $k_f$  and the chromatic aberration in the CTEM will lead to an additional phase shift in  $\chi(\theta)$

which can be compensated for by refocusing or raising the incident beam voltage by the energy loss  $\Delta E$ .

Fig. 2 shows the spatial dependence of  $P(b, E)$  for typical “large” and small collector apertures calculated using Eq. (13). The donut shape characteristic of the small (1.5 mrad) collector is lost when the collector is the same size or larger than the objective aperture. It is the  $A_{\perp}$  terms that give rise to the donut shape. Both  $A_{\perp}$  and  $A_{\parallel}$  decay as  $1/\beta^2$  for large  $\beta$  (i.e.  $\beta > \theta_E, \theta_0$ ) so the contribution to  $P(b, E)$  from a small collector of area  $(\Delta\beta)^2$  and placed far off axis at  $\beta = (\beta_x, \beta_y)$  is

$$P(b, E) = \frac{k_0^4 (\Delta\beta)^2 R_y}{4\pi^4 E_0} \times |A_{\parallel}|^2 \left[ \theta_E^2 |k_0 z_{\text{fi}}|^2 + \beta^2 |k_0 x_{\text{fi}}|^2 \right], \quad (20)$$

as  $\beta^2 |A_{\parallel}|^2 \gg |A_{\perp}|^2$ . This means the perpendicular component of the scattering will no longer drop to zero at small impact parameters (as  $A_{\perp}$  does) but instead tends to a large finite value of a form similar to Eq. (12). This reduces the height of the donut and as a rough rule of thumb, when  $\beta_0^2 + \theta_E^2 \geq \theta_0^2$ , the donut shape is washed out completely.

### 3.5. Atomic resolution with plasmons?

If the collector is displaced far enough off axis so that it no longer overlaps with the objective aperture and  $\beta^2 \gg \theta_0^2$  for all  $\beta$  then Eq. (20) takes on the remarkable form [25]

$$P(b, E) = \frac{R_y}{E_0} \left( \frac{\Delta\beta^2}{\beta^4} \right) \left[ \theta_E^2 |k_0 z_{\text{fi}}|^2 + \beta^2 |k_0 x_{\text{fi}}|^2 \right] |a(b)|^2. \quad (21)$$

This is to say that the inelastic scattering is just as localized as the incident probe intensity, independent of the energy loss! (The only spatial dependence is that of the probe wave function  $a(b)$ ). To see why this should be, recall that the denomi-

nator of  $A_{\parallel}$  comes from the Coulomb potential (Eq. (16)):

$$4\pi e^2 V(\mathbf{K}) = \frac{4\pi e^2}{K^2} = \frac{4\pi e^2}{k_0^2 (\theta_E^2 + (\beta - \theta)^2)}. \quad (22)$$

This is very similar to the form factor for elastic scattering from a screened Coulomb potential where  $\epsilon(q, 0)$  is approximated by the Thomas-Fermi dielectric function [26]:

$$V(\mathbf{K}) = \frac{1}{\epsilon(q, 0)} \frac{4\pi e^2}{K^2} \approx \frac{4\pi e^2}{\theta_{\text{TF}}^2 + (\beta - \theta)^2}. \quad (23)$$

For most materials, the characteristic Thomas-Fermi scattering angle,  $\theta_{\text{TF}}$ , is comparable to the objective aperture cutoff at 100 kV so  $V(\mathbf{K})$  varies little in the integration over scattering angle in Eq. (13). Since  $V(\mathbf{K})$  is roughly constant, its Fourier transform in real space must be localized, i.e. on the scale of the probe wave function  $V(r) \sim \delta(r)$  so the elastic scattering appears localized and the resolution limit for ADF imaging is determined only by the probe wave function [27–29].

Inelastic scattering can also be localized by displacing the collector so  $\beta \gg \theta_0$ . Then  $V(\mathbf{K})$  is independent of  $\theta$  and

$$V(\mathbf{K}) \approx \frac{4\pi e^2}{\theta_E^2 + \beta^2} \Rightarrow V(r) \approx \frac{4\pi e^2}{\theta_E^2 + \beta^2} \delta(r). \quad (24)$$

Fig. 3a shows a comparison of  $P(b, \Delta E = 25$  eV) for a small collector on-axis and a small collector displaced to almost  $3\theta_0$ . By displacing the collector, the signal has been made localized but weak. Effectively the Coulomb potential has been high-pass-filtered to form a “weak beam” inelastic image. The idea of displacing the collector aperture to obtain a more localized signal has been used by Taftø and Krivanek [30] in diffraction and channeling experiments. Ritchie and Howie [2] have estimated the extent of localization for the parallel component of the scattering for small collector displacements where the effect is noticeable but not quite as dramatic. From Eq. (21) it is clear that the parallel component decays as the inverse of the fourth power of the scattering angle so the signal is very weak for a collector

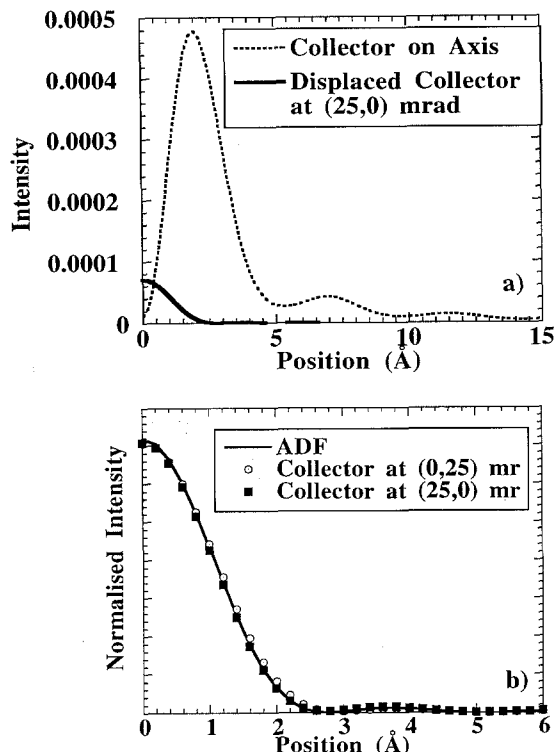


Fig. 3. Calculated  $P(b, \Delta E = 25 \text{ eV})$  for (a) a point detector on-axis and a point detector displaced 25 mrad in a direction parallel to the impact parameter. (b) Displacing the collector off axis makes the inelastic signal as localized as the incident probe. Whether the collector is displaced in a direction parallel (25, 0) or perpendicular (0, 25) to the impact parameter makes no difference for large displacements. Conditions for a 100 kV STEM with  $C_s = 3.3 \text{ mm}$ , 1100 Å defocus and a 8.18 mrad objective aperture.

displacement sufficient to localize the inelastic scattering. In contrast, the perpendicular component of the inelastic scattering decays as the inverse of the second power of the scattering angle so a usable signal is still present. It is interesting to note that the elastic signal also decays like the parallel component of the inelastic scattering, i.e. as  $1/\beta^4$ . So there should be a range of scattering angles where the perpendicular component of the inelastic scattering should dominate the elastic scattering. At large enough scattering angles, the quadrupole scattering will become significant as this signal will be roughly independent of the scattering angle. For plasmon

maps formed in this way, the large momentum transfer will mean that the plasmons can be damped by single particle excitations [31], and the resultant lifetime broadening will lower the energy resolution. For amorphous materials where the crystal momentum is not a good quantum number to begin with, this effect should be small. Strong plural scattering will limit this method to thin specimens and it is important to exclude any diffracted beams from the collector aperture as in conventional weak-beam imaging.

#### 4. Experiment

Some of the features of the inelastic scattering described above are quite general, especially those that can be recovered from the classical argument. For instance the inelastic signal is expected to decay exponentially at large distances from the scattering target with a decay length  $b_{\text{max}}/2$ . This is a function of the energy loss alone and is not determined by the nature of the excitation (classical, quantum, single particle or collective) or the specimen shape. The specimen and probe shapes, however, are important for determining the behavior of  $P(b, E)$  at small distances. For instance while a single dipole has a spatial dependence of  $P(b, E) \propto K_0^2(b/b_{\text{max}}) + K_1^2(b/b_{\text{max}})$ , summing the responses of a line of dipoles gives  $P(b, E) \propto K_1(2b/b_{\text{max}})$  [17]. If a half space is filled with dipoles,  $P(b, E) \propto K_0(2b/b_{\text{max}})$  [17] which varies as  $P(b, E) \propto -\ln b$  at small  $b$  instead of  $P(b, E) \propto 1/b^2$  for an isolated dipole. (Note that all have the same long-range behaviour as explained in Section 3.1).

##### 4.1. Measurement of the inelastic decay length

A simple illustration of the decay of the inelastic scattering or the “dynamic screening” follows the experiment of Isaacson, Langmore and Rose [6] where the energy loss of a STEM probe is recorded as the probe is brought in from the vacuum to the edge of a thin film. Here we use a VG-HB501A 100 kV STEM with serial EELS and placed within a shielded room [32]. The

results for a thin Si film covered by SiO<sub>2</sub> are shown in Fig. 4a and for an a-C film (the support grid for a graphite test specimen) in Fig. 4b. The data spans 5 orders of magnitude and is really only made possible by using digital single electron pulse counting where the thermal background averaged less than 1 count for the 20 ms dwell time used. Each energy loss line scan is recorded simultaneously with the ADF signal [33] so the edge of the specimen could be determined. The magnification was calibrated using the silicon (111) fringes for Fig. 4a and the graphite (0002)

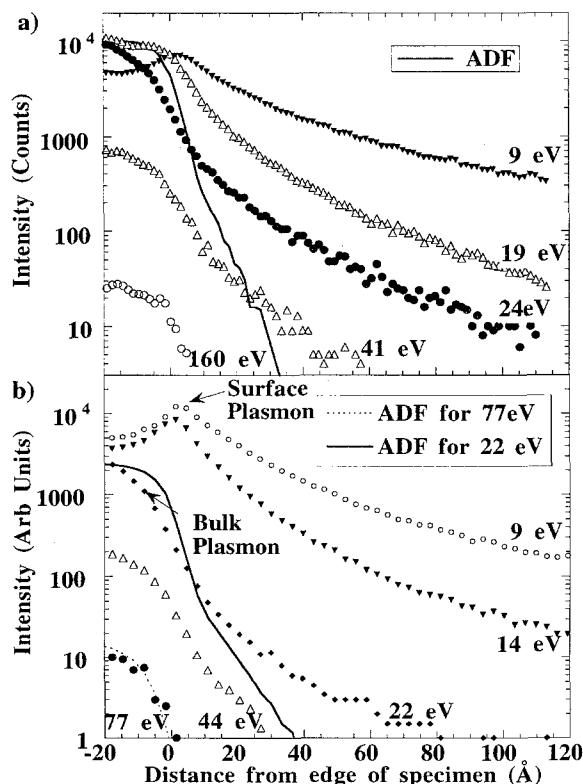


Fig. 4. Experimentally measured line scans of inelastic scattering intensity,  $P(b, E)$ , as a function of distance from the edge of the specimen. (a)  $P(b, E)$  for a thin SiO<sub>2</sub> layer at the end of a silicon wedge. (b)  $P(b, E)$  for a thin (30 Å) a-C support grid showing pronounced surface plasmons at 9, 14 eV. Notice that the bulk plasmon at 22 eV has a reduced intensity at the edge of the specimen where oscillator strength has been transferred to the surface modes. Both data sets recorded on a VG-HB501A with  $C_s = 3.3$  mm, 50  $\mu$ m objective aperture and 10 mrad collector aperture.

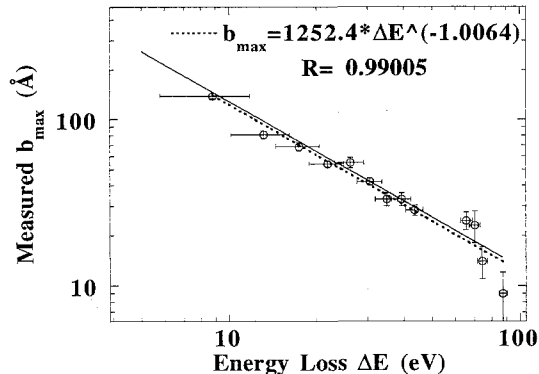


Fig. 5. Measured inelastic decay length  $b_{\max}$  for different energy losses. For  $b \gg b_{\max}$  we expect  $P(b, E) \propto \exp(-2b/b_{\max})$ . This is evident in Fig. 4 where  $P(b, E)$  for a given  $E$  follows a straight line on a log-linear scale at large distances. Thus  $b_{\max}$  can be measured from the slope of  $P(b, E)$  versus  $b$  for a fixed energy loss  $E$ . Here measured  $b_{\max}$  values (from the data of Fig. 4a) are plotted against the energy loss  $E$ . The solid diagonal line is the theoretical (and relativistic)  $b_{\max} = \gamma v / \omega = 1293 / E$  and the dashed line is the least-squares fit to the experimental data ( $R$  is the linear correlation coefficient). The two are within experimental error.

fringes for Fig. 4b. At large distances from the specimen the signal was found to decay as  $\exp(-2b/b_{\max})$  to within the 3% experimental error (Fig. 5.) The main sources of systematic error are the residual uncertainties in the position and energy scales.

Comparing the theoretical and measured spatial dependences of  $P(b, E)$  for small distances is more difficult as we really do not know what the specimen shape is. One possibility is to exploit the incoherent imaging conditions obtained by using a large collector (Eq. (8)). The convolution of the specimen with the probe shape can be determined by simultaneously recording the ADF signal with the inelastic signal. The expected inelastic signal can then be modeled by convolving the ADF signal with the inelastic response of a single dipole  $w_D(\rho, \rho, E)$  (calculated with a finite cutoff angle). Fig. 6 shows the comparison of a plasmon line scan across the edge of a thin carbon film with the expected inelastic signal. The only free parameter was the overall intensity as both the energy loss and horizontal scale are

determined by the experimental conditions. Overall the agreement is good and the largest discrepancy is at about 20 Å into the specimen where the model has overestimated the bulk plasmon intensity. This is expected as the bulk plasmon is suppressed at the surface but the convolution implies that the bulk plasmon response is uniform throughout the specimen.

#### 4.2. “Weak beam” inelastic imaging with a displaced collector

The calculations of Section 3.4 suggest that when the collector is displaced off axis so it no longer overlaps with the objective aperture or any of the Bragg beams, the inelastic scattering should be just as localized as the probe wave function. To test this idea we must minimize the effects of plural scattering and multiple elastic scattering which will degrade the spatial resolution. The multiple elastic scattering can be minimized by using an amorphous specimen that is thin enough that only kinematic scattering need be considered. The ratio of inelastic to elastic scattering,  $(\sigma_i/\sigma_E)$ , can be enhanced by working with light elements since  $(\sigma_i/\sigma_E)$  is inversely proportional to the atomic number [27]. For carbon  $(\sigma_i/\sigma_E) \approx 3$  [34].

Fig. 7 shows line scans recorded in the carbon plasmon loss ( $P(b, \Delta E = 25 \text{ eV})$ ) for both an

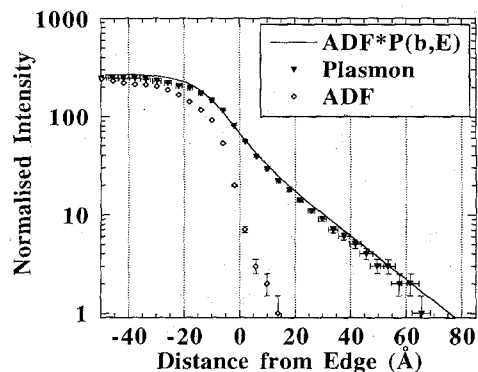


Fig. 6. Comparison of the experimentally measured carbon plasmon loss at 25 eV with the theoretical  $P(b, \Delta E = 25 \text{ eV})$  obtained by convolving  $w(\rho, \rho', E)$  with the ADF signal (see text). Data recorded on a VG-HB501A with  $C_s = 3.3 \text{ mm}$ ,  $50 \mu\text{m}$  objective aperture and 10 mrad collector aperture.

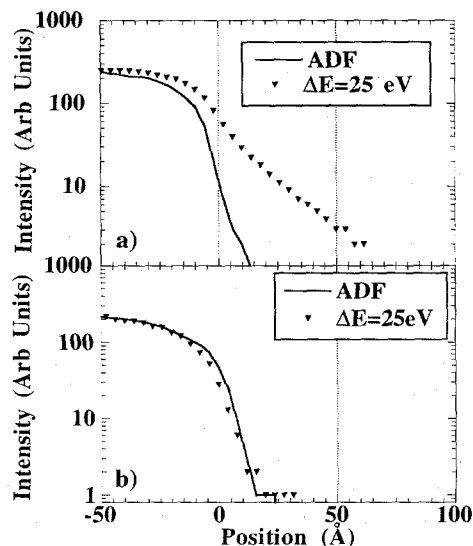


Fig. 7. The effect of displacing the collector aperture to form a “weak beam” inelastic image: (a) shows a measured line scan recorded in the carbon plasmon loss for a thin ( $< 30 \text{ Å}$ ) carbon film with a 10 mrad collector centered on the optic axis and the simultaneously recorded ADF signal; (b) the collector is displaced 25 mrad off axis using the Grigson coils to form the weak beam image. The measured plasmon line scan with the displaced collector is as localized as its simultaneously recorded ADF signal, i.e. the resolution of the weak beam inelastic image is determined by the probe shape alone. (Data recorded on a VG-HB501A with  $C_s = 3.3 \text{ mm}$ ,  $50 \mu\text{m}$  objective aperture and 10 mrad collector aperture.)

on-axis and a displaced collector aperture. The specimen is the edge of a carbon support grid, less than  $30 \text{ Å}$  thick. It is clear from Fig. 7b that the inelastic “weak beam” image with the displaced collector has the same spatial resolution as the simultaneously recorded ADF image. The only difference between the weak-beam plasmon scan and the ADF image is that the plasmon intensity is less at the surface of the film. This is a strong indication that the main contribution to the weak-beam image is from the bulk plasmon as this has a reduced intensity at the surface.

## 5. Discussion

The theory discussed in this paper has so far only considered single inelastic scattering and the

experiments have been chosen to satisfy that condition as closely as possible. In this regime, we found quantitative agreement between theory and experiment. Under more typical conditions, multiple scattering and dielectric screening in the bulk must also be considered.

For instance would the spatial dependence of the scattering from a dipole be changed if a slab of some conducting material were placed between the dipole and the probe? Dielectric screening can only improve the spatial resolution of an inelastic image for very low energy losses (typically quarter to a tenth of the bulk plasmon loss). In the Landau theory of a charged Fermi liquid, the static screening length,  $\lambda_s$ , is given exactly in the long-wavelength limit as  $\lambda_s = s/\omega_p$  [31] where  $s$  is the macroscopic sound velocity and  $\omega_p$  is the classical plasma frequency. From the plasmon dispersion relationship  $\omega^2 = \omega_p^2 + s^2q^2$  we can deduce that the dielectric screening length for excitations below the plasma frequency is  $\lambda = s/\sqrt{\omega_p^2 - \omega^2}$  and that there is no dielectric screening for energy losses at and above the plasmon frequency. (A similar result could be obtained by screening a test charge with the dielectric response of a medium that satisfies the hydrodynamic limit at long wavelengths.) Consequently a bulk plasmon cannot screen itself. Nor would we expect the spatial variation of an energy loss due to say a dipole embedded in this medium to be very different from its spatial variation in free space if the energy loss is greater than that of plasma frequency. This is simply a realization that the system can respond above its resonant frequency. For instance the measured EELS signal due to a Si  $L_{2,3}$  edge at 99 eV from a silicon impurity in aluminium would decay as  $\exp(-b/b_{\max})$  at large distances from the impurity just as if the impurity were in vacuo. However, the signal from say a valence excitation of the impurity silicon particle below the resonant frequency of the bulk aluminium might be expected to fall off more rapidly than it would in free space.

The effect of multiple elastic scattering on the inelastic image recorded with a small on axis collector (or a CTEM with a small condenser angle) has been discussed in Section 3.2. The

main effect will be a preservation of diffraction contrast effects (such as thickness fringes) which will have to be deconvolved in order to isolate the inelastic scattering. The situation is more hopeful for imaging with a large collector aperture. If the detector is large enough to collect almost all the inelastically scattered electrons the resulting image is incoherent. In many respects this image is very similar to the ADF signal. To see this, consider the elastic scattering from a single Thomas–Fermi atom. Using the elastic scattering form factor of Eq. (23) in Eq. (3) and taking the limit of a large detector (with the unscattered beam removed by having a small hole in the center) the probability of elastic scattering is

$$P_E(b) \propto |a(\mathbf{b})|^2 \otimes |K_0(b/\lambda_{TF})z_{ii}|^2, \quad (25)$$

while that for single inelastic scattering with a similar (but energy filtering) detector is given by Eq. (9):

$$P_D(b, E) \propto |a(\mathbf{b})|^2 \otimes \left[ |K_0(b/b_{\max})z_{fi}|^2 + |K_1(b/b_{\max})x_{fi} \cos \gamma|^2 \right]. \quad (26)$$

In other words, for single scattering, the parallel component of inelastic scattering has the same spatial dependence as elastic scattering from a Thomas–Fermi atom. Provided all the scattered electrons are collected, the multiple scattering corrections for both Eqs. (25) and (26) should be very similar [35] and much of our understanding of probe channeling in ADF can also be applied here. Effects associated with the depth of penetration due to channeling [36], development of “forbidden” periodicities [37] and strain field scattering [38,39,37] are all likely to arise and may complicate interpretation.

Some typical measures of spatial resolution for the inelastic scattering are shown in Fig. 8. These are based on the full quantum mechanical calculation of Eq. (13). The full width at half maximum (FWHM) is only slightly worse than that of the incident probe and not particularly sensitive to the energy loss. The main effect of the inelastic delocalization is to add slowly decaying tails to the point spread function which become progressively worse at lower energies. This is reflected in the rapid broadening of the disk containing 80%

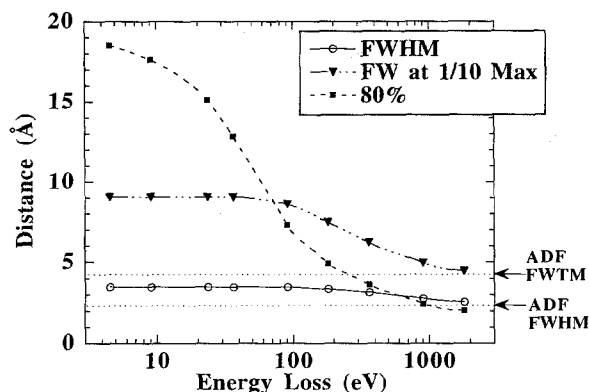


Fig. 8. Measures of spatial resolution for a 100 kV STEM at 1100 Å defocus with  $C_s = 3.3$  mm, a 8.18 mrad objective aperture and a 10 mrad collector aperture. The full width at half maximum (FWHM), full width at tenth maximum and the radius of the disk containing 80% of the scattered electrons are shown for  $P(b, E)$  from a single dipole, calculated using Eq. (13).

of the scattered electrons. At large energy losses (where  $b_{\max}$  is less than the probe size) the resolution is determined only by the incident probe size. It may seem surprising that the FWHM and the FWTM (full width at tenth of the maximum) are also constant for small energy losses. However, this is expected from the semiclassical model. If the probe size is much smaller than  $b_{\max}$  then for  $b < b_{\max}$ ,  $P(b, E) \propto 1/b^2$ . As a power-law decay has no characteristic length scale, measures such as the FWHM, FWTM and the rms impact parameter must be independent of the energy loss. It is only the breakdown of the semiclassical approximation at the impact parameter  $b_{\min} = 1$  Å (which is determined by the probe size) that prevents  $P(b, E)$  from diverging and determines the scale at small distances. Only when  $b_{\max} \leq nb_{\min}$  and  $P(b, E)$  begins to decay exponentially will the full width at  $n$ th maximum become energy dependent which occurs at  $\sim 100$  eV in Fig. 8.

## 6. Conclusions

How delocalized is inelastic scattering? Fig. 1 showed that under typical imaging conditions,

even plasmon maps can have subnanometer spatial resolution while Fig. 4 showed that inelastic signal also has an exponentially decaying character at large distances. The lesson is that for analytical work where the resolution limit might be taken as the full width at tenth maximum, the signal is quite delocalized. However, for imaging, where the signal/noise is worse, and the full width at half maximum is a better criterion, then the inelastic scattering is almost always localized to within 5 Å.

Classically, the energy loss of a fast electron is a function of the impact parameter. Quantum mechanically, the energy loss is independent of the impact parameter, but the probability of the occurrence of that loss is not and using the correspondence principle it must vary as  $P(b, E_i) \cdot E_i = \Delta E_{\text{classical}}(b)$ . Bohr's adiabatic criterion  $b_{\max} = v/\omega$  gives the experimentally measured decay length for inelastic scattering and plays the same role as the dielectric screening length does in elastic scattering from a Thomas–Fermi atom. In fact the parallel component of the inelastic scattering from a dipole has the same spatial dependence as elastic scattering from a Thomas–Fermi atom.

The role of the detector in inelastic scattering is the same as in elastic scattering – a small collector leads to a coherent image (an axial dark-field signal) while a using a large collector results in incoherent imaging. Ideally,  $\theta_c \approx 3\theta_0$  for incoherent imaging, but such a large collection angle often degrades the energy resolution of the spectrometer. However, provided the collection angle is greater than the objective angle, the imaging conditions are closer to incoherent than coherent (i.e. the bright-field signal should resemble the complement of the ADF signal).

Displacing the collector aperture to form an inelastic “weak beam” image makes the resolution of an energy loss image comparable to that of the annular dark-field image. The delocalization is more pronounced at higher beam energies so the “weak beam” imaging should prove useful for obtaining subnanometer resolution plasmon maps in 200 and 300 kV electron microscopes.

Finally it should be noted that the spatial localization of the inelastic scattering (as a result

of the exponential decay at large distances) depends only on the energy loss measured, rather than a detailed knowledge of the nature of the material. This suggests it may be possible to remove the “blurring” of an inelastic image by deconvolution using Eq. (13) as the impulse response of the system. This assumes the specimen is thin, dipole scattering dominates and a sufficiently good signal-to-noise ratio can be achieved at the higher spatial frequencies of the probe. In practise, this last condition is probably the limiting one [44].

### Acknowledgments

This research was supported by the Department of Energy (Grant DE-FG02-87ER45322). The Cornell UHV STEM was acquired through the NSF(Grant #DMR-8314255) and is operated by the Cornell Materials Science Center (NSF grant#DMR-9121654). Support and helpful discussions with Earl Kirkland and Mick Thomas are also acknowledged. Comments by P. Batson, H. Kohl, A. Howie, P. Echenique, H. Bethe and R. Egerton were also appreciated.

### Appendix A. Quantum mechanical derivation of $P(b, E)$

We start by calculating the transition rate for the fast electron wavepacket to excite the target system from its ground state to some excited state and for which the fast electron loses an energy  $\Delta E$ . This is given by Fermi's golden rule

$$\Gamma_{i \rightarrow f} = \frac{2\pi}{\hbar} |\langle \psi_f | V | \Psi_i \rangle|^2 \delta(E_i - E_f - \Delta E). \quad (\text{A.1})$$

The initial state  $|\Psi_i\rangle = |\phi_i\rangle |\varphi_p\rangle$  is taken as the product of the ground state wave function of the target,  $|\phi_i\rangle$ , and the probe wave function  $|\varphi_p\rangle$ . Exchange between the target electrons and the probe electron can be ignored as there is little overlap in momentum space between the bound and incident electrons [40]. Usually the probe is

assumed to be sufficiently large that it can be approximated by a single plane wave. This leads to Bethe's theory of inelastic scattering [16] which is reviewed in Ref. [41]. For a probe of atomic dimensions we must describe the wavepacket (centered around impact parameter  $b$ ) by a coherent superposition of plane waves:

$$\langle r | \varphi_p \rangle = \frac{1}{(2\pi)^2 \sqrt{L}} \int d\mathbf{k} A(\mathbf{k}) e^{i\mathbf{k} \cdot (\mathbf{r} - b)}, \quad (\text{A.2a})$$

and for single scattering we can consider the final state to be a plane wave:

$$\langle \varphi_f | \mathbf{r} \rangle = \frac{e^{-i\mathbf{k}_f \cdot \mathbf{r}}}{L^{3/2}}, \quad (\text{A.2b})$$

where the wave functions have been normalized in a box of length  $L$ .

The interaction Hamiltonian is the Coulomb potential

$$V(\mathbf{r}) = - \sum_{j=1}^Z \frac{e^2}{|\mathbf{r} - \mathbf{r}_j|} + \frac{Z}{|\mathbf{r} - \mathbf{r}_N|}, \quad (\text{A.3})$$

where  $\mathbf{r}_j$  are the coordinates of the bound electrons and  $\mathbf{r}_N$  is the position of the atomic nucleus (if we are considering scattering from a single atom). As we will be interested in transmitted rather than backscattered electrons we can ignore the nuclear contribution (2nd term) as the energy transfer is then small. We can then write the matrix element as

$$\begin{aligned} \langle \psi_f | V | \psi_i \rangle &= \frac{-1}{(2\pi)^2 L^2} \int d\mathbf{k} A(\mathbf{k}) e^{-i\mathbf{k} \cdot b} \int d\mathbf{r} \\ &\times \left\langle \varphi_f \left| \sum_{j=1}^Z \frac{e^2}{|\mathbf{r} - \mathbf{r}_j|} \right| \varphi_i \right\rangle e^{-i\mathbf{k} \cdot \mathbf{r}}, \end{aligned} \quad (\text{A.4})$$

where the scattering vector  $\mathbf{K} = \mathbf{k}_f - \mathbf{k}$ . The integration over  $\mathbf{r}$  can be done using Bethe's integral [16]

$$\int d\mathbf{r} \frac{1}{|\mathbf{r} - \mathbf{r}_j|} e^{-i\mathbf{K} \cdot \mathbf{r}} = \frac{4\pi}{K^2} e^{i\mathbf{K} \cdot \mathbf{r}_j}. \quad (\text{A.5})$$

The matrix element can then be rewritten as

$$\langle \psi_f | V | \psi_i \rangle = \frac{-1}{(2\pi)^2 L^2} \int d\mathbf{k} A(\mathbf{k}) A(\mathbf{k}) e^{-i\mathbf{k} \cdot \mathbf{b}} \\ \times \frac{4\pi e^2}{K^2} \left\langle \varphi_f \left| \sum_{j=1}^Z e^{-i\mathbf{K} \cdot \mathbf{r}_j} \right| \varphi_i \right\rangle. \quad (\text{A.6})$$

It is then customary at this point to introduce the Fourier transform of the particle density

$$\rho(\mathbf{K}) = \sum_{j=1}^Z e^{-i\mathbf{K} \cdot \mathbf{r}_j}, \quad (\text{A.7})$$

so the matrix elements of the density fluctuations become

$$\rho(\mathbf{K})_{f,i} = \left\langle \varphi_f \left| \sum_{j=1}^Z e^{-i\mathbf{K} \cdot \mathbf{r}_j} \right| \varphi_i \right\rangle. \quad (\text{A.8})$$

The density matrix is useful for treating single particle and many body excitations on an equal footing. Later it will become necessary to expand the density matrix in powers of  $K$  in order to study the specific forms of  $P(b, E)$ . When we do so, the single particle excitations will provide simple and concrete examples.

We are now in a position to calculate  $P(b, E)$ . First we use (A.8) and (A.6) in (A.1) to obtain the transition rate to all final states such that  $k_f$  lies within the detector

$$\Gamma = \frac{2\pi}{\hbar} \sum_{k_f} \left( \frac{e^2}{\pi L^2} \right)^2 \\ \times \int d\mathbf{k}, d\mathbf{k}' A(\mathbf{k}) A^*(\mathbf{k}') e^{-i(\mathbf{k}-\mathbf{k}') \cdot \mathbf{b}} \\ \times \frac{\rho(\mathbf{K})_{i,f}}{K^2} \frac{\rho(\mathbf{K}')_{i,f}^+}{K'^2} \delta(E_i - E_f - \Delta E) \\ = \frac{e^4}{4\pi^4 \hbar L} \\ \times \int d\mathbf{k}_f, d\mathbf{k}, d\mathbf{k}' D(\mathbf{k}_f) A(\mathbf{k}) A^*(\mathbf{k}') \\ \times e^{-i(\mathbf{k}-\mathbf{k}') \cdot \mathbf{b}} \\ \times \frac{\rho(\mathbf{K})_{i,f}}{K^2} \frac{\rho(\mathbf{K}')_{i,f}^+}{K'^2} \delta(E_i - E_f - \Delta E). \quad (\text{A.9})$$

The second line follows from introducing a detector function  $D(k)$  that is 1 inside the collector aperture and 0 outside, and replacing the sum over final states by an integral  $\sum_{k_f} \rightarrow \int d\mathbf{k}_f / (2\pi/L)^3$ . If the wavepacket travels at group velocity  $v = \hbar k_0 / m$  then the probability that an excitation occurs is the transition rate (A.9) multiplied by the interaction time  $L/v$  so

$$P(b, E) = \frac{1}{2\pi^4} \left( \frac{R_y}{k_0} \right) \int d\mathbf{k}_f, d\mathbf{k}, d\mathbf{k}' \\ \times D(\mathbf{k}_f) A(\mathbf{k}) A^*(\mathbf{k}') e^{-i(\mathbf{k}-\mathbf{k}') \cdot \mathbf{b}} \\ \times \frac{\rho(\mathbf{K})_{i,f}}{K^2} \frac{\rho(\mathbf{K}')_{i,f}^+}{K'^2} \delta(E_i - E_f - \Delta E), \quad (\text{A.10})$$

where  $R_y = e^2 / 2a_0$  is the Rydberg energy and  $a_0 = \hbar^2 / me^2$  is the Bohr radius.

So far the expression for  $P(b, E)$  is exact (within the first Born approximation). To proceed further we assume the energy loss  $\Delta E \ll E_0$  and make the usual small angle approximations [5]. This is done by writing the scattering vectors in a Taylor series of the scattering angles and neglecting terms of second order or higher. This has the effect of converting the Ewald spheres to planes parallel to the optic axis (see Fig. 9). We can then write

$$\mathbf{K} = k_0 [\theta_E \hat{z} + (\boldsymbol{\beta} - \boldsymbol{\theta})], \\ \mathbf{K}' = k_0 [\theta_E \hat{z} + (\boldsymbol{\beta}' - \boldsymbol{\theta}')], \quad (\text{A.11})$$

where the perpendicular components of  $k_0$  and  $k_f$  are  $k_0 \boldsymbol{\theta}$  and  $k_0 \boldsymbol{\beta}$ , respectively. The  $z$ -component of the scattering vectors  $\mathbf{K}, \mathbf{K}'$ , is the  $k_0 \theta_E$  where  $\theta_E$  is fixed by integrating over the  $z$ -component of  $k_f$  in (A.10). This follows from  $|k_f| \approx |k_0|(1 - \theta_E)$  so

$$\Delta E = \frac{\hbar^2}{2m} (k_0^2 - k_f^2) = \frac{\hbar^2}{2m} (2k_0^2 \theta_E + \vartheta(\theta_E^2)) \\ \approx 2E_0 \theta_E. \quad (\text{A.12})$$

The delta function in (A.10) which is required by conservation of energy becomes

$$\delta(E_i - E_f - \Delta E) = \frac{1}{2E_0} \delta \left( \theta_E - \frac{E_i - E_f}{2E_0} \right). \quad (\text{A.13})$$

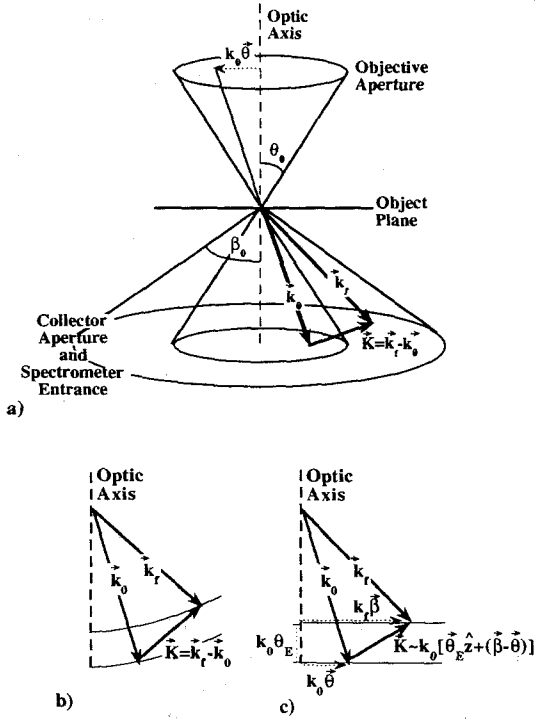


Fig. 9. (a) Scattering geometry in a STEM. (b) Energy conservation fixes the initial and final wavevectors to lie on spheres of radius  $k_0 = \sqrt{(2m/\hbar^2)E_0}$  and  $|k_f| = \sqrt{(2m/\hbar^2)E_0(1 - \Delta E/E_0)}$ , respectively. (c) The small angle approximations changes these spheres into two planes,  $k_0 \Delta E / 2E_0$  apart. The parallel and perpendicular components of momentum transfer,  $K$ , are also shown.

We now use  $\Delta E$  as a shorthand for  $E_i - E_f$ . The integration over the delta function will set  $\theta_E = \Delta E / 2E_0$

The probe wave function of Eq. (A.2) becomes

$$a(\mathbf{r} - \mathbf{b}) = \frac{e^{ik_0 z}}{2\pi^2} \int d^2(k_0 \theta) A(\theta) e^{ik_0 \theta \cdot (\rho - \mathbf{b})}, \quad (\text{A.14})$$

where  $\mathbf{r} = (\rho_x, \rho_y, z)$ ,

$$A(\theta) = \begin{cases} C e^{i\chi(\theta)} & \text{for } |\theta| \leq \theta_0, \\ 0 & \text{otherwise,} \end{cases} \quad (\text{A.15})$$

with  $C = 1/(k_0 \theta_0 \sqrt{\pi})$ .

$$\chi(\theta) = k_0 \left( (C_s/4)\theta^4 - (\Delta f/2)\theta^2 \right) \quad (\text{A.16})$$

describes the phase shift due to the objective lens.  $C_s$  is the coefficient of spherical aberration and  $\Delta f$  is the defocus. The constant in  $A(\theta)$ , is introduced so the integrated probe intensity in real space is normalized to one. Substitution of (A.11)–(A.16) into (A.10) gives a result similar to that obtained by Kohl and Rose [5]:

$P(b, E)$

$$= \frac{k_0^4}{4\pi^4} \left( \frac{R_y}{E_0} \right) \int d^2\beta d^2\theta d^2\theta' D(\beta) A(\theta) \times A^*(\theta') e^{-ik_0(\theta - \theta') \cdot \mathbf{b}} \frac{\rho(\mathbf{K})_{i,f}}{K^2} \frac{\rho(\mathbf{K}')_{i,f}^+}{K'^2}, \quad (\text{A.17})$$

where  $D(\beta)$  is 0 outside the detector and 1 for  $\beta < \beta_0$ . The multiplication of the density matrices  $\rho(K)$  and  $\rho(K')$  leads to cross-terms in  $K \cdot K'$  so this equation is not in general separable into independent integrals over  $\theta$  and  $\theta'$ . Kohl and Rose [5] introduce a mixed dynamic form factor to make the coherent nature of this integration explicit.

Eq. (A.17) has closed forms for 2 special cases, a STEM with a very large detector and CTEM or STEM with a point BF detector which are best illustrated by expressing Eq. (A.17) in terms of real space variables:

$$A(\theta) = \int a(\rho) e^{ik_0 \theta \cdot \rho} d^2\rho, \quad (\text{A.18})$$

$$\frac{\rho(\mathbf{K})_{i,f}}{K^2} \frac{\rho(\mathbf{K}')_{i,f}^+}{K'^2} = \int w(\rho, \rho', E) e^{-i(\mathbf{K} \cdot \rho - \mathbf{K}' \cdot \rho')} d^2\rho d^2\rho'. \quad (\text{A.19})$$

Here  $\bar{\rho}$  is the perpendicular component of  $\rho$ , not to be confused with the density matrix  $\rho(K)$ .  $w(\rho, \rho', E)$  has been called the ‘‘cross spectral object transparency’’ by Rose [21] and is defined by the inverse Fourier transform of Eq. (A.19):

$$w(\rho, \rho', E) = \left( \frac{1}{2\pi} \right)^2 \int \frac{\rho(\mathbf{K})_{i,f}}{K^2} \frac{\rho(\mathbf{K}')_{i,f}^+}{K'^2} \times e^{i(\mathbf{K} \cdot \rho - \mathbf{K}' \cdot \rho')} d^2\mathbf{K} d^2\mathbf{K}'. \quad (\text{A.20})$$

Specific forms of  $w(\boldsymbol{\rho}, \boldsymbol{\rho}', E)$  are discussed in Appendix B.

Substituting Eqs. (A.18) and (A.19) in (A.17) and using the integral representation of the delta function

$$\int d\boldsymbol{\theta} e^{-ik_0\boldsymbol{\theta}\cdot(\boldsymbol{\rho}-\boldsymbol{\rho}')} = \frac{4\pi^2}{k_0^2} \delta(\boldsymbol{\rho}-\boldsymbol{\rho}') \quad (\text{A.21})$$

eliminates  $K$  and  $\theta$  so  $P(b, E)$  can be expressed in terms of real spaces variables alone:

$$\begin{aligned} P(b, E) &= \frac{4R_y}{E_0} \int a(\boldsymbol{\rho}-\mathbf{b}) a^*(\boldsymbol{\rho}'-\mathbf{b}) w(\boldsymbol{\rho}, \boldsymbol{\rho}', E) \\ &\quad \times D(\boldsymbol{\rho}-\boldsymbol{\rho}') d^2\boldsymbol{\rho} d^2\boldsymbol{\rho}', \end{aligned} \quad (\text{A.22})$$

which is the desired result for Eq. (3).

If we then assume the collector aperture is circular and centered on the optic axis then the integral over  $\beta$  can also be performed:

$$\begin{aligned} D(\boldsymbol{\rho}-\boldsymbol{\rho}') &= \int D(\beta) e^{-ik_0\beta\cdot(\boldsymbol{\rho}-\boldsymbol{\rho}')} d^2\beta \\ &= \int_0^{\beta_0} \int_0^{2\pi} \beta e^{-ik_0\beta_0|\boldsymbol{\rho}-\boldsymbol{\rho}'|\cos\phi} d\phi d\beta \\ &= \frac{2\pi\beta_0^2 J_1(k_0\beta_0|\boldsymbol{\rho}-\boldsymbol{\rho}'|)}{k_0\beta_0|\boldsymbol{\rho}-\boldsymbol{\rho}'|}. \end{aligned} \quad (\text{A.23})$$

The scattering probability can then be expressed more compactly as

$$\begin{aligned} P(b, E) &= \frac{4R_y}{E_0} \int a(\boldsymbol{\rho}-\mathbf{b}) a^*(\boldsymbol{\rho}'-\mathbf{b}) w(\boldsymbol{\rho}, \boldsymbol{\rho}', E) \\ &\quad \times \frac{2\pi\beta_0^2 J_1(k_0\beta_0|\boldsymbol{\rho}-\boldsymbol{\rho}'|)}{k_0\beta_0|\boldsymbol{\rho}-\boldsymbol{\rho}'|} d^2\boldsymbol{\rho} d^2\boldsymbol{\rho}'. \end{aligned} \quad (\text{A.24})$$

## Appendix B. $w(\boldsymbol{\rho}, \boldsymbol{\rho}', E)$ for a dipole excitation

The ‘‘cross spectral object transparency’’ of Rose [21]  $w(\boldsymbol{\rho}, \boldsymbol{\rho}', E)$  is essentially the impulse response of the system to the probe wavepacket and plays a similar role to the transmission func-

tion of classical optics [42]. From its definition (Eq. (8)) it can also be thought of as a density cross correlation function in real space:

$$\begin{aligned} w(\boldsymbol{\rho}, \boldsymbol{\rho}', E) &= \left( \frac{1}{2\pi} \right)^2 \int \frac{\rho(\mathbf{K})_{i,f}}{K^2} \frac{\rho(\mathbf{K}')_{i,f}^*}{K'^2} \\ &\quad \times e^{i(\mathbf{K}\cdot\boldsymbol{\rho}-\mathbf{K}'\cdot\boldsymbol{\rho}')} d^2\mathbf{K} d^2\mathbf{K}'. \end{aligned} \quad (\text{B.1})$$

Usually a thermal average over the density matrices is taken but for simplicity we ignore such effects and assume that the system is initially prepared in one specific state  $|\phi_i\rangle$ .

To consider a specific form of  $w$  we expand the density matrices  $\rho(\mathbf{K})_{i,f}$  in powers of  $(\mathbf{K}\cdot\mathbf{r}_j)$ .

$$\begin{aligned} \rho(\mathbf{K})_{f,i} &= \langle \varphi_f | \varphi_i \rangle - i \langle \varphi_f | \mathbf{K}\cdot\mathbf{r}_j | \varphi_i \rangle \\ &\quad - \langle \varphi_f | (\mathbf{K}\cdot\mathbf{r}_j)^2 | \varphi_i \rangle + \dots \end{aligned} \quad (\text{B.2})$$

The leading term  $\langle \varphi_f | \varphi_i \rangle = 0$  as the initial and final states are orthogonal. In general, if  $(\mathbf{K}\cdot\mathbf{r}_j)$  is small then it is only necessary to consider the dipole contribution. However, the upper limit of the integral over  $K$  in (B.1) is the maximum momentum transferred to the system which could be as much as  $k_0$ . The probability of such an event occurring is very small and almost all the intensity is contained within the Bethe ridge [40]. The cutoff angle at the Bethe ridge is  $\theta_c \approx \sqrt{2\theta_E}$ . For a typical low loss excitation  $\theta_c \approx 14$  mrad so the small-angle approximation of Eq. (2) is still accurate but the momentum transfer at the cutoff angle would be  $k_c \approx 2.4 \text{ \AA}^{-1}$  so the non-dipole terms are not negligible. Spatially these higher-order terms dominate only at very small distances. Their behavior can be generalized from the calculated dipole contribution. Eq. (B.2) can be simplified by making the small-angle approximation and choosing the  $x$ -axis to lie along the dipole

$$\begin{aligned} \rho(\mathbf{K})_{f,i} &= -ik_0[\theta_E z_{if} + \alpha \cos(\phi) x_{if}] \\ &\quad - k_0^2[\theta_E^2 z_{if}^2 + 2\theta_E \alpha \cos(\phi) z_{if} x_{if} \\ &\quad + \alpha^2 \cos^2(\phi) x_{if}^2] + \dots, \end{aligned} \quad (\text{B.3})$$

where  $\phi$  is the angle between the  $x$ -axis and the component of  $K$  perpendicular to the optic axis which is  $k_0\alpha = k_0(\beta - \theta)$ . The matrix elements

are abbreviated as  $z_{\text{if}}^n = \langle \varphi_f | z^n | \varphi_i \rangle$ . Keeping only the dipole contribution (the first term in (B.3)) and substituting into (B.1) we get

$$\begin{aligned} w(\boldsymbol{\rho}, \boldsymbol{\rho}', E) &= \left( \frac{k_0}{2\pi} \right)^2 \int \frac{[\theta_E z_{\text{if}} + \alpha \cos \phi x_{\text{if}}]}{\theta_E^2 + \alpha^2} \\ &\times \frac{[\theta_E z_{\text{if}}^* + \alpha' \cos \phi' x_{\text{if}}^*]}{\theta_E^2 + \alpha'^2} \\ &\times e^{ik_0(\boldsymbol{\alpha} \cdot \boldsymbol{\rho} - \boldsymbol{\alpha}' \cdot \boldsymbol{\rho}')} d^2\boldsymbol{\alpha} d^2\boldsymbol{\alpha}', \end{aligned} \quad (\text{B.4})$$

where  $\gamma$  is the angle between  $\boldsymbol{\rho}$  and the  $x$ -axis so  $\boldsymbol{\alpha} \cdot \boldsymbol{\rho} = \alpha\rho \cos(\gamma - \phi)$ . Notice that the integral over the primed variables is separable and the complex conjugate of the integral over the unprimed variables. Rewriting  $\cos \phi$  as a sum of exponentials and making a change of variable from  $\phi$  to  $\eta = \gamma - \phi$  we find

$$\begin{aligned} w(\boldsymbol{\rho}, \boldsymbol{\rho}', E) &= \left( \frac{k_0}{2\pi} \right)^2 \int d\alpha \frac{\alpha}{\theta_E^2 + \alpha^2} \int_0^{2\pi} d\eta \\ &\times [z_{\text{if}}\theta_E e^{ik_0\alpha\rho \cos \eta} + \chi_{\text{if}}\alpha(e^{ik_0\alpha\rho \cos \eta - i\gamma + i\eta} \\ &+ e^{ik_0\alpha\rho \cos \eta + i\gamma - i\eta})/2] \times \text{C.C.}(\boldsymbol{\rho}'). \end{aligned} \quad (\text{B.5})$$

The inner integral can be evaluated since the Bessel functions  $J_m$  can be written as [43]

$$J_m(x) = \frac{1}{2\pi i^m} \int_0^{2\pi} d\eta e^{ix \cos \eta - im\eta}, \quad (\text{B.6})$$

so the first term of the inner integral will be proportional to  $J_0$  while the second will be proportional to  $iJ_1$  and  $-iJ_{-1}$ . Since  $J_1 = -J_{-1}$  we find

$$\begin{aligned} w(\boldsymbol{\rho}, \boldsymbol{\rho}', E) &= \frac{k_0^2}{2\pi} \int d\alpha \left[ z_{\text{if}}\theta_E \frac{\alpha}{\theta_E^2 + \alpha^2} J_0(k_0\rho\alpha) \right. \\ &\left. + ix_{\text{if}} \cos \gamma \frac{\alpha^2}{\theta_E^2 + \alpha^2} J_1(k_0\rho\alpha) \right] \times \text{C.C.}(\boldsymbol{\rho}'). \end{aligned} \quad (\text{B.7})$$

In the limit  $k_0\rho \rightarrow \infty$  Eq. (B.7) has a closed form.

This can be seen by making a change of variable to  $x = k_0\rho\alpha$  and using the integral [43]

$$\int_0^\infty \frac{x^{v+1}}{x^2 + a^2} J_v(bx) dx = a^v K_v(ab), \quad (\text{B.8})$$

which gives the dipole form of  $w_{\text{D}}(\boldsymbol{\rho}, \boldsymbol{\rho}', E)$ :

$$\begin{aligned} w_{\text{D}}(\boldsymbol{\rho}, \boldsymbol{\rho}', E) &= \frac{(k_0\theta_E)^2}{2\pi} [K_0(k_0\rho\theta_E) z_{\text{if}} \\ &+ iK_1(k_0\rho\theta_E) x_{\text{if}} \cos \gamma] [K_0(k_0\rho'\theta_E) z_{\text{if}}^* \\ &- iK_1(k_0\rho'\theta_E) x_{\text{if}}^* \cos \gamma']. \end{aligned} \quad (\text{B.9})$$

When  $P(b, E)$  is calculated by integrating over  $\boldsymbol{\rho}$  and  $\boldsymbol{\rho}'$  (such as in Eq. (9)) the symmetry between the integral over  $\boldsymbol{\rho}$  and that over  $\boldsymbol{\rho}'$  means cross terms between the perpendicular and parallel components of the dipole excitation in (B.9) will cancel and the only non-zero terms will be

$$\begin{aligned} w_{\text{D}}(\boldsymbol{\rho}, \boldsymbol{\rho}', E) &= \frac{(k_0\theta_E)^2}{2\pi} [K_0(k_0\rho\theta_E) K_0(k_0\rho'\theta_E) |z_{\text{if}}|^2 \\ &+ K_1(k_0\rho\theta_E) K_1(k_0\rho'\theta_E) \\ &\times \cos \gamma \cos \gamma' |x_{\text{if}}|^2]. \end{aligned} \quad (\text{B.10})$$

Returning to Eq. (B.3), the quadrupole contribution will be

$$\begin{aligned} w_{\text{Q}}(\boldsymbol{\rho}, \boldsymbol{\rho}', E) &= \frac{(k_0\theta_E)^4}{2\pi} [K_0(k_0\rho\theta_E) K_0(k_0\rho'\theta_E) |z_{\text{if}}^2|^2 \\ &+ K_2(k_0\rho\theta_E) K_2(k_0\rho'\theta_E) \cos^2 \gamma \cos^2 \gamma' \\ &\times bvx_{\text{if}}^2|^2 + 2K_1(k_0\rho\theta_E) K_1(k_0\rho'\theta_E) \\ &\times \cos \gamma \cos \gamma' |z_{\text{if}}x_{\text{if}}|^2]. \end{aligned} \quad (\text{B.11})$$

We are now in a position to examine the validity of the dipole approximation used in Eqs. (7)–(11) of the main text. The dipole approximation assumes a small momentum transfer and hence a small scattering angle. However, in transforming to real space, we integrate over all scattering angles. As long as the contribution from large scattering angles is small, the dipole term will dominate. For a valence-shell excitation, the matrix elements will be of the order of  $(a_0^n)^2$  for

the  $n$ th order multipole. As all the modified Bessel functions decay exponentially at large enough distances, the ratio of quadrupole to dipole scattering for  $b \gg b_{\max}$  will be

$$\frac{w_Q(\boldsymbol{\rho}, \boldsymbol{\rho}, E)}{w_D(\boldsymbol{\rho}, \boldsymbol{\rho}, E)} = (k_0 a_0 \theta_E)^2 = \left( \frac{a_0}{b_{\max}} \right)^2. \quad (\text{B.12})$$

Only above a few keV energy loss (i.e. when  $\Delta E \approx E$ ) does the quadrupole scattering become comparable to the dipole scattering.

At small distances  $K_n(x) \propto 1/x^n$  except for  $K_0$  which diverges logarithmically so to leading order, the ratio of quadrupole to dipole scattering for  $b \gg b_{\max}$  will be

$$\frac{w_Q(\boldsymbol{\rho}, \boldsymbol{\rho}, E)}{w_D(\boldsymbol{\rho}, \boldsymbol{\rho}, E)} = \left( \frac{a_0}{\rho} \right)^2. \quad (\text{B.13})$$

The quadrupole scattering is only significant for impact parameters of the same size as the dipole matrix elements which are typically of subatomic dimensions. The quadrupole scattering need be considered at all only if these spatial frequencies are transmitted by the microscope. For an on-axis detector, the dipole approximation is good below a few keV energy loss and at all but the closest distances. This should be expected as the total cross section calculated by integrating the impact parameter based cross section over all space gives the same result as the Bethe formula.

## References

- [1] N. Bohr, *Phil. Mag.* 25 (1913) 10.
- [2] R. Ritchie and A. Howie, *Phil. Mag.* A 58 (1988) 753.
- [3] M. Scheinfein, A. Muray and M. Isaacson, *Ultramicroscopy* 16 (1985) 233.
- [4] C. Colliex, O.L. Krivanek and P. Trebbia, in: *EMAG 81 [Inst. Phys. Conf. Ser. 61 (1981) 183]*.
- [5] H. Kohl and H. Rose, *Adv. Electron. Electron Phys.* 65 (1985) 173.
- [6] M. Isaacson, J.P. Langmore and H. Rose, *Optik* 41 (1974) 92.
- [7] P.E. Batson, *Surf. Sci.* 156 (1985) 720.
- [8] D. Ugarte, C. Colliex and P. Trebbia, *Phys. Rev. B* 45 (1992) 4332.
- [9] P.E. Batson, *Nature* 366 (1993) 727.
- [10] N.D. Browning, M.M. Chisholm and S.J. Pennycook, *Nature* 366 (1993) 143.
- [11] D.A. Muller, Y. Tzou, R. Raj and J. Silcox, *Nature* 366 (1993) 725.
- [12] E. Fermi, *Z. Physik* 29 (1924) 315.
- [13] N.F. Mott, *Proc. Camb. Phil. Soc.* 27 (1931) 533.
- [14] J.W. Frame, *Proc. Camb. Phil. Soc.* 27 (1931) 511.
- [15] J.A. Gaunt, *Proc. Camb. Phil. Soc.* 23 (1927) 732.
- [16] H. Bethe, *Ann. Physik* 5 (1930) 325.
- [17] J.P.R. Bolton and L.M. Brown, *Proc. Roy. Soc. (London)* A 428 (1990) 291.
- [18] M. Sunjic and A.A. Lucas, *Phys. Rev. B* 3 (1971) 719.
- [19] P.M. Echenique and J.B. Pendry, *J. Phys. C* 8 (1975) 2936.
- [20] J.D. Jackson, *Classical Electrodynamics* (Wiley, New York, 1976) ch. 13.
- [21] H. Rose, *Ultramicroscopy* 15 (1984) 173.
- [22] E.J. Williams, *Proc. Roy. Soc. A* 139 (1933) 163.
- [23] C. Bertulani and G. Baur, *Phys. Today* 47 (March 1994) 22.
- [24] A. Howie, *Proc. Roy. Soc. (London)* A 271 (1963) 268.
- [25] To obtain Eq. (21) from Eq. (19), note that the  $V(\mathbf{K})$  of Eq. (24) can be taken outside the integrals of Eqs. (14) and (15) which then reduce to the probe wave function by using Eq. (A.14).
- [26] N.W. Ashcroft and N.D. Mermin, *Solid State Physics* (Saunders College, Philadelphia, 1976) p. 340.
- [27] A.V. Crewe, J.P. Langmore and M.S. Isaacson, in: *Physical Aspects of Electron Microscopy and Microbeam Analysis*, Eds. B.M. Siegel and D.R. Beaman (Wiley, New York, 1975) p. 47.
- [28] G. Black and E.H. Linfoot, *Proc. Roy. Soc. (London)* A 239 (1957) 522.
- [29] D.A. Kopf, *Optik* 59 (1981) 89.
- [30] J. Taftø and O.J. Krivanek, *Phys. Rev. Lett.* 48 (1982) 560.
- [31] D. Pines and P. Nozieres, *The Theory of Quantum Liquids*, Vol. 1 (Addison-Wesley, New York, 1989).
- [32] J. Silcox, P. Xu and R.F. Loane, *Ultramicroscopy* 47 (1992) 173.
- [33] E.J. Kirkland, *Ultramicroscopy* 32 (1990) 349.
- [34] R.F. Egerton, *Phys. Status Solidi (a)* 37 (1976) 663.
- [35] S.E. Hillyard, R.F. Loane and J. Silcox, *Ultramicroscopy* 49 (1993) 14.
- [36] S.E. Hillyard and J. Silcox, *Ultramicroscopy* 52 (1993) 325.
- [37] S.E. Hillyard and J. Silcox, *Ultramicroscopy* 58 (1995) 6.
- [38] D.D. Perovic, C.J. Rossow and A. Howie, *Ultramicroscopy* 52 (1993) 353.
- [39] J. Liu and J.M. Cowley, *Ultramicroscopy* 52 (1993) 3335.
- [40] J.J. Sakurai, *Modern Quantum Mechanics* (Addison Wesley, New York, 1985).
- [41] M. Inokuti, *Rev. Mod. Phys.* 43 (1971) 297.
- [42] M. Born and E. Wolf, *Principles of Optics*, 6th ed. (Pergamon, New York, 1980) p. 481–490.
- [43] I.S. Gradshteyn and I.M. Ryzhik, *Tables of Integrals, Series and Products*, 4th ed. (Academic Press, New York, 1980).
- [44] H. Kohl and A. Berger, *Ultramicroscopy* 59 (1995) 191.